# Linköping University Post Print


# Ti-Si-C-N Thin Films Grown by Reactive Arc Evaporation from $Ti_3SiC_2$ Cathodes


Anders Eriksson, Jianqiang Zhu, Naureen Ghafoor, Jens Jensen, Grzegorz Greczynski, Mats Johansson, Jacob Sjölen, Magnus Odén, Lars Hultman and Johanna Rosén



N.B.: When citing this work, cite the original article.



Original Publication:

Anders Eriksson, Jianqiang Zhu, Naureen Ghafoor, Jens Jensen, Grzegorz Greczynski, Mats Johansson, Jacob Sjölen, Magnus Odén, Lars Hultman and Johanna Rosén, Ti-Si-C-N Thin Films Grown by Reactive Arc Evaporation from $Ti_3SiC_2$ Cathodes, 2011, Journal of Materials Research, (26), 874-881.
http://dx.doi.org/10.1557/jmr.2011.10


Copyright: Mrs Materials Research Society
http://www.mrs.org/

Postprint available at: Linköping University Electronic Press
http://urn.kb.se/resolve?urn=urn:nbn:se:liu:diva-61992

# Ti–Si–C–N thin films grown by reactive arc evaporation from $Ti_3SiC_2$ cathodes

Anders O. Eriksson[a)]
*Thin Film Physics Division, Department of Physics, Chemistry, and Biology (IFM), Linköping University, SE-581 83 Linköping, Sweden*

Jianqiang Zhu and Naureen Ghafoor
*Nanostructured Materials, Department of Physics, Chemistry, and Biology (IFM), Linköping University, SE-581 83 Linköping, Sweden*

Jens Jensen and Grzegorz Greczynski
*Thin Film Physics Division, Department of Physics, Chemistry, and Biology (IFM), Linköping University, SE-581 83 Linköping, Sweden*

Mats P. Johansson
*Nanostructured Materials, Department of Physics, Chemistry, and Biology (IFM), Linköping University, SE-581 83 Linköping, Sweden; and Seco Tools AB, SE-737 82 Fagersta, Sweden*

Jacob Sjölen
*Seco Tools AB, SE-737 82 Fagersta, Sweden*

Magnus Odén
*Nanostructured Materials, Department of Physics, Chemistry, and Biology (IFM), Linköping University, SE-581 83 Linköping, Sweden*

Lars Hultman and Johanna Rosén
*Thin Film Physics Division, Department of Physics, Chemistry, and Biology (IFM), Linköping University, SE-581 83 Linköping, Sweden*

(Received 18 November 2010; accepted 4 January 2011)

Ti–Si–C–N thin films were deposited onto WC-Co substrates by industrial scale arc evaporation from $Ti_3SiC_2$ compound cathodes in $N_2$ gas. Microstructure and hardness were found to be highly dependent on the wide range of film compositions attained, comprising up to 12 at.% Si and 16 at.% C. Nonreactive deposition yielded films consisting of understoichiometric $TiC_x$, Ti, and silicide phases with high (27 GPa) hardness. At a nitrogen pressure of 0.25–0.5 Pa, below that required for N saturation, superhard, 45–50 GPa, (Ti,Si)(C,N) films with a nanocrystalline feathered structure were formed. Films grown above 2 Pa displayed crystalline phases of more pronounced nitride character, but with C and Si segregated to grain boundaries to form weak grain boundary phases. In abundance of N, the combined presence of Si and C disturbs cubic phase growth severely and compromises the mechanical strength of the films.

## I. INTRODUCTION

Transition metal carbides and nitrides are successfully employed as wear- and oxidation-resistant thin films. The research trend is toward multinary compounds to achieve film materials with enhanced and optimized properties for various applications. In this study, we report on the Ti–Si–C–N system, inspired by and extending the limits of the two successfully applied ternaries Ti–Si–N[1] and Ti–C–N.[2] The quarternary system is challenging in terms of the several binary and ternary phases that it comprises, as well as unresolved issues about element substitution and segregation in the different phases. While the Ti–C–N system exhibits complete solid solubility in the B1 cubic phase, the Ti–Si–N system is characterized by strong segregation of Si to form TiN and polymorphic Ti–Si and $Si_3N_4$ phases. Mixing all four elements may also give rise to competing SiC and $CN_x$ formation. These effects are highly dependent on composition, as shown in this work.

The Ti–Si–C–N system has been explored to some extent in thin films made by chemical vapor deposition (CVD),[3–6] plasma enhanced CVD (PECVD),[7–10] and magnetron sputtering from various Ti–Si–C compound targets[11,12] or Ti targets used in trimethylsilane $(CH_3)_3SiH$ and $N_2$.[13,14] Magnetron sputtering of Si has also been combined with arc deposition of Ti in an atmosphere with $CH_4$ and $N_2$.[15] Cathodic arc is known to produce dense and defect-rich films in processes that can be readily applied at an industrial scale. However, it is only recently that arc-deposited films in the Ti–Si–C–N system have

a)Address all correspondence to this author.
e-mail: ander@ifm.liu.se
DOI: 10.1557/jmr.2011.10

 © Materials Research Society 2011

been reported, resulting from deposition processes with conventional Ti–Si compound cathodes used in a mixture of $N_2$ and $CH_4$ in an industrial scale system [16] as well as in combination with $N_2$ and $C_2H_2$ in a smaller system.[17]

In this study, we advance beyond standard cathode materials and report on reactive arc evaporation from ternary $Ti_3SiC_2$ cathodes in $N_2$ gas. The use of compound cathodes is of interest for rational utilization of coating equipment and simple process control, compared to setups with a multitude of elemental cathodes. Our method offers relatively high concentrations of Si and C, while maintaining the high film density and crystallinity characteristic of arc deposition. We thus present a path to explore carbonitride films with a unique range of compositions and structures.

## II. EXPERIMENTAL DETAILS

Thin films were deposited from ternary $Ti_3SiC_2$ cathodes (Maxthal) of a so-called MAX phase,[18] prepared in bulk form and commercially available. A schematic of the industrial scale cathodic arc evaporation system (Sulzer Metaplas MZR 323) is shown in Fig. 1. Polished cemented carbide substrates, S, of WC with 10 wt.% Co were placed on a cylinder rotating at 3 rpm about 15 cm in front of the cathodes, operated at an arc current of 50 A dc. The substrates were negatively biased at $-30$ V. The chamber was heated through resistive heating elements located on the far chamber side to a temperature of $\sim$400 °C on the rotating cylinder. Nitrogen was introduced at pressures between 0 and 6 Pa, to form a reactive atmosphere. During nonreactive deposition, a small addition of Ar, $\sim$0.1 Pa, was needed to sustain the arc. The deposition pressure of $N_2$ is hereafter abbreviated $pN_2$. The base pressure was $\sim 10^{-3}$ Pa and all films were deposited to a thickness in the range 3–5 μm.

Film and cathode compositions were analyzed by elastic recoil detection analysis with a time-of-flight and energy detector (TOF-E ERDA), using a 40 MeV $^{127}I^{9+}$ ion beam at 22.5° incidence angle relative to the surface. The resulting time-of-flight versus recoil energy spectra were evaluated using the CONTES code.[19]

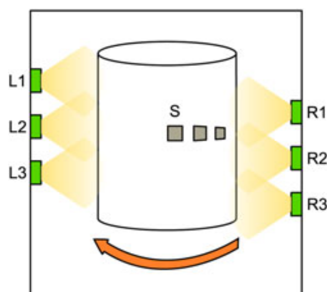


FIG. 1. Schematic drawing of the deposition system. Cathodes are denoted L1–L3 and R1–R3, and substrates are denoted S.

X-ray diffractometry (XRD) for phase analysis was performed using a Bruker AXS D8-advanced x-ray diffractometer with a line-focus Cu $K_\alpha$ x-ray source. $\theta$-2$\theta$ scans were recorded in the 2$\theta$-range from 2 to 80°. Structural characterization was performed through transmission electron microscopy (TEM) using an analytical FEI Tecnai G2 TF 20 UT microscope equipped with an energy dispersive x-ray spectrometer. Cross-sectional TEM (XTEM) samples were prepared through mechanical polishing and ion milling. Surface morphology was characterized using a LEO 1550 scanning electron microscope (SEM) operated at 5 kV.

Chemical bonding state analysis through x-ray photoelectron spectroscopy (XPS) was performed in a Scienta ESCA200 spectrometer, using a monochromatized Al($K_\alpha$) x-ray source with photon energy $h\nu$ = 1486.6 eV. The samples were not sputter cleaned prior to measurement to avoid preferential sputtering and sputter-induced chemistry. The graphite C1s position at 284.6 eV was used as reference for the energy calibration and a Shirley-type background subtraction was used in data analysis.

Film hardness was measured on polished tapered cross sections, using a UMIS nanoindenter equipped with a Berkovich diamond tip. Approximately 20 indents were made for each sample to an indentation depth of $\sim$0.2 μm, corresponding to a maximum applied load of 15–40 mN. Hardness was evaluated using the method proposed by Oliver and Pharr.[20]

## III. RESULTS AND DISCUSSION

### A. Composition

Figure 2(a) shows the composition of the Ti–Si–C–N films as a function of $N_2$ deposition pressure. All films are rich in Si and C, with compositions in the range 10–12 and 16–28 at.%, respectively. Arcing from $Ti_3SiC_2$ cathodes without reactive gas yielded films with 10 at.% Si and 28 at.% C, which is lower compared to the cathode composition; the latter was confirmed by ERDA within a few at.% of the nominal composition of 17 at.% Si and 33 at.% C. The compositional difference between cathode and film can, at least in part, be attributed to preferential resputtering.[21] The N content increases with increase in $N_2$ pressure up to 37 at.% at $pN_2$ = 2 Pa. Further increase in pressure gives only small compositional changes, and the system is therefore considered to have reached a point of saturation. Films grown in the presence of $N_2$ have lower concentrations of Ti and C if compared to the $pN_2$ = 0 Pa deposition. The decrease is slightly larger than predicted from the plain effect of dilution. For the samples deposited at $pN_2$ = 2–6 Pa, $\sim$38 at.% Ti would be expected if the ratios between Ti, Si, and C were preserved from the $pN_2$ = 0 Pa deposition, which contrasts the measured 34 at.%. The Si content remains relatively stable at 10–12 at.%

throughout the whole series. Using an alternative notation, see Table I, the film with maximum Si content, deposited at $pN_2$ = 0.5 Pa, can also be described as $(Ti_{0.77}Si_{0.23})(C_{0.35}N_{0.65})_{0.88}$. The compositional ratio between C and N on the one side and Ti and Si on the other side varies considerably from 0.42 in the sample deposited without $N_2$ up to 1.29 when the highest $N_2$ pressure was used. The apparent overstoichiometry, with respect to TiN and TiC, at high $pN_2$ can be explained by the presence of $Si_3N_4$, $CN_x$, and related phases that coordinate more N than the cubic (Ti,Si)(C,N) phase, as discussed later. The indicated N content at $pN_2$ = 0 Pa in Table I corresponds to ~1 at.%, as presented in Fig. 2. This is below the level of O contamination of 1–4 at.% present in all samples. However, both C and O can be slightly overestimated in ERDA analysis because of rough sample surfaces. The Si and C contents exceed the values reported from arcing TiSi cathodes (compromising up to 20 at.% Si) in $CH_4$ and $N_2$, where the maximum incorporation of Si and C was in $(Ti_{0.86}Si_{0.14})(C_{0.28}N_{0.72})_{0.87}$.[16] The use of ternary cathodes is thus one way to extend the range of attainable compositions in Ti–Si–C–N films grown by arc deposition. Beyond this method, PECVD synthesis of C-rich films with Si contents up to 11.6 at.% have been reported. This corresponds to $(Ti_{0.77}Si_{0.23})(C_{0.77}N_{0.23})_{0.95}$, with a microstructure composed of Ti(C,N), SiC, and $Ti_2C$ phases.[22] As shown later, the films investigated in this study consist primarily of cubic (Ti,Si)(C,N) phase. The Si and C contents are henceforth presented in at% of total composition, as given in Fig. 2(a).

The compositional variations determined by ERDA are strongly correlated to film hardness, as shown in Fig. 2(b). The hardness maximum is found for films deposited at $pN_2$ = 0.25 and 0.5 Pa, which corresponds to intermediate N-content. However, a detailed interpretation of these results also requires investigation of microstructure and chemical bonding, as presented later.

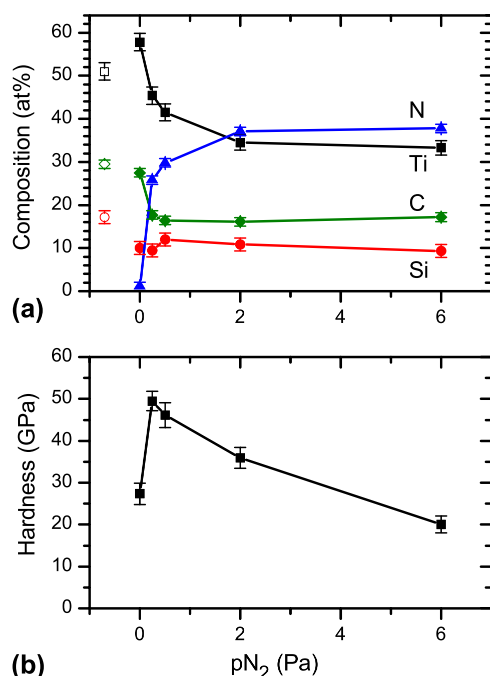


FIG. 2. (a) Film composition in at.% as a function of $N_2$ deposition pressure (the cathode composition is indicated by open symbols) and (b) film hardness.

## B. Microstructure and nanostructure

Results from XRD analysis are presented in Fig. 3. In addition to peaks from the WC-Co substrate, the sample deposited without reactive gas shows a broad feature in the region from 30 to 50° (2θ). Its maximum, in a broad plateau at 41–42°, encompasses the reference position of the TiC 200 peak, as well as peaks from Ti, $Ti_5Si_3$, and $TiSi_2$.[23] The presence of these metallic and silicide phases is supported by XPS data presented later. An additional small peak located at 2θ = 61° overlaps with TiC. No signs of $Ti_3SiC_2$ were found for measurements down to 2θ = 5°, which is unsurprising since the film composition deviates from the MAX-phase stoichiometry also for nonreactive growth. The broad XRD-peaks can be explained by stress or small crystallite size on the nanometer scale, the latter as evidenced by high resolution TEM (HRTEM).

TABLE I. Film composition expressed as stoichiometry factors in $(Ti_{1-x}Si_x)(C_yN_{1-y})_z$.

| Deposition $N_2$ pressure (Pa) | Si/(Ti + Si) ($x$) | C/(C + N) ($y$) | (C + N)/(Ti + Si) ($z$) |
|---|---|---|---|
| 0 | 14.7% | 96.2% | 0.42 |
| 0.25 | 17.2% | 40.7% | 0.79 |
| 0.5 | 22.8% | 35.5% | 0.88 |
| 2 | 23.8% | 30.7% | 1.18 |
| 6 | 21.8% | 31.3% | 1.29 |

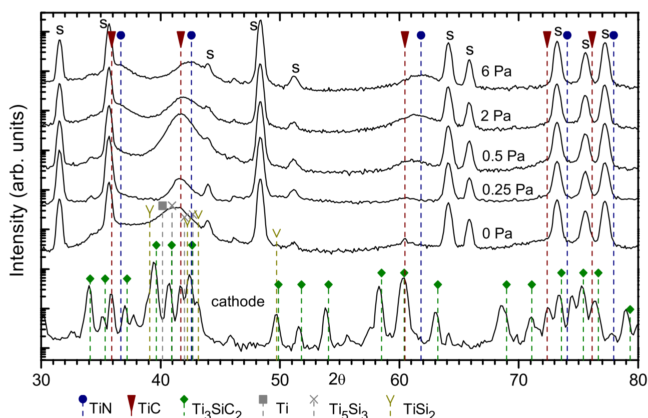


FIG. 3. X-ray diffractometry pattern from Ti–Si–C–N films and the $Ti_3SiC_2$ cathode. S denotes substrate peak.

For films deposited in a $N_2$ environment, more distinct peaks appear corresponding to an fcc-structure with lattice parameters between references for TiC and TiN.[23] The 200 peak at ~42° has a maximum intensity for films deposited at $pN_2 = 0.5$ Pa. The 111 peak at 36–37° partly overlaps with a substrate peak and the most visible shoulder is in the two samples deposited at $pN_2 = 2$ and 6 Pa. The 220 peak, identified at 61–62°, also has substantial broadening. A small shift of this peak toward higher angles can be observed with increasing N content. This is likely to be the effect of a decreasing lattice parameter as N replaces C in the cubic structure, though concomitant change in the intrinsic stress level cannot be ruled out. Although distinct XRD peaks without substrate overlap is required for exact stress measurements, the present $\sin^2\psi$ measurements of the 200 peaks indicate a substantial compressive stress of 5–7 GPa, assuming an E-modulus of 450 GPa.[24] We also note that Si substituting for Ti in TiN does not give detectable shifts in the lattice parameter.[1]

Figure 4 shows dark field (to the left) and high resolution (to the right) XTEM micrographs from films deposited at different $N_2$ pressures. At $pN_2 = 0$ Pa [Fig. 4(a)], the structure is fully crystalline and comprises 2–7 nm large equiaxed grains. The film exhibits a 002 preferred crystallographic orientation, as indicated by the selected area electron diffraction (SAED) pattern, in agreement with the XRD results. For the film deposited at $pN_2 = 0.25$ Pa, shown in Fig. 4(b), the microstructure is columnar with ~10–15 nm wide grains, resulting again in the 002 texture.

At $pN_2 = 0.5$ Pa, shown in Fig. 4(c), a feather-like microstructure appears. It consists of bundles of nano-size crystallites fanning out from the substrate normal, as can be seen in both the dark-field and HRTEM modes. The trace of {200} lattice planes of two diverging grains are indicated in the figure. This nanostructure with semicoherent crystallites has previously been observed in arc-deposited Ti–Si–N[1,25] and Ti–Si–C–N[16] films. The suggested explanation involves Si segregation on the coating surface, which leads to repeated renucleation of (002)-textured Ti(C)N subgrains and eventual $Si_3N_4$ precipitation. Si-vacancy-stabilized cubic-like $SiN_x$ ($x \approx 1.33$) may also form in contact with TiN.[1,26,27] The pronounced 002 texture in the films deposited at $pN_2 = 0.5$ Pa is similar to what was reported by Flink et al.[1]

At the highest N content ($pN_2 = 6$ Pa), the sample consists of fine grains of a few nanometers [Fig. 4(d)]. Low-density areas at apparent column boundaries were visible in underfocused bright-field imaging (not shown here). The HRTEM imaging indicates a fine-grained defect-rich structure without voids, but with possible amorphous domains. Any amorphous phase, however, would have very minor volume fraction of the material, as the SAED diffraction pattern features only fcc reflections, but no amorphous rings. A coarser (50-nm scale) STEM imaging in Fig. 5(a) shows that there exists a superimposed, apparently columnar, structure along the growth direction, with 3–5 nm wide rod-like features. The rod contrast suggests that these areas consist of elements lighter than Ti. The banded horizontal layering visible in the image, and present in all samples investigated, is an effect of sample rotation in the high-capacity commercial

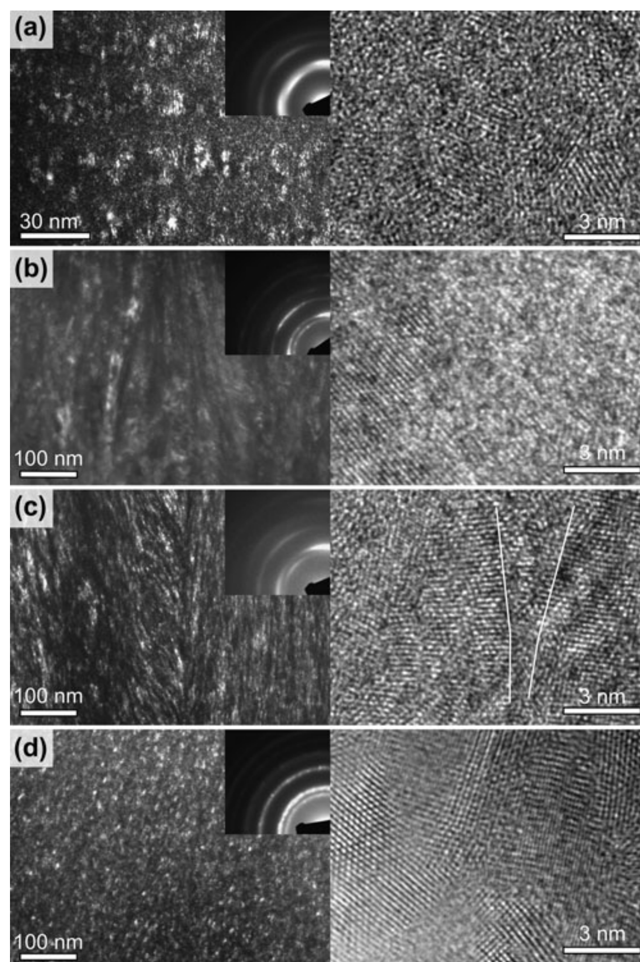


FIG. 4. Dark-field transmission electron micrographs (TEM) with corresponding selected area electron diffraction pattern insets (to the left) and high resolution TEM images (to the right) of samples grown with $pN_2$ equal to (a) 0 Pa, (b) 0.25 Pa, (c) 0.5 Pa, and (d) 6 Pa. The trace of {200} lattice planes of two grains is indicated in (c).

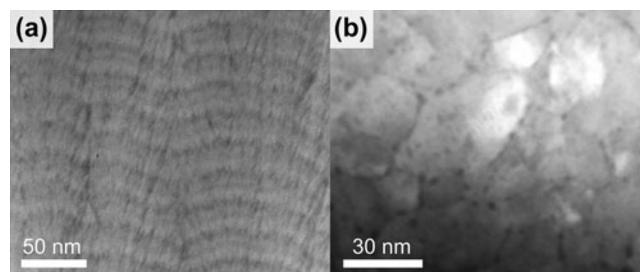


FIG. 5. (a) Scanning TEM of a $pN_2 = 6$ Pa sample, indicating segregation of light elements as dark rods in cross section. (b) In plan view, the light elements appear at grain boundaries.

coating systems, as described in detail elsewhere.[21] We note that the rod-like features track valleys in the film surface in each stage of deposition, indicated by the layers. In plan view STEM [Fig. 5(b)], we see that the light element areas decorate the grain boundaries. Hence, the extremely fine-grained structure and the rod-like features in the $pN_2 =$ 6 Pa film is a strong indication that Si and possibly C segregate at the film surface during growth and reacts to some extent with N supplied from the gas ambient.

### C. Chemical bonding state

XPS peak profiles for Ti2p, Si2p, C1s, and N1s core levels are presented in Figs. 6(a)–6(d). The Ti2p spectra in Fig. 6(a) are the most complex one since there are two asymmetrical core level lines ($Ti2p_{3/2}$ and $Ti2p_{1/2}$) associated with each chemical state of the Ti atom. However, the spin split between $Ti2p_{3/2}$ and $Ti2p_{1/2}$ signals is ~6 eV, i.e., larger than the accounted chemical shifts, which facilitates analysis. We base the discussion on the $Ti2p_{3/2}$ core levels that comprise the binding energy region between 452 and 459 eV. The corresponding $Ti2p_{1/2}$ signals appear at the binding energies higher than 459 eV and are not referred to in the text below. In the case of Si2p, the energy split between $Si2p_{3/2}$ and $Si2p_{1/2}$ core level components is smaller than the experimental resolution; hence, there is a one-to-one correspondence between spectral features and chemical states of the Si atom.

The sample deposited without $N_2$ shows peaks corresponding to Ti–C bonds at 454 eV in the $Ti2p_{3/2}$ spectra and at ~281 eV in the C1s spectra. There is likely a fraction of Ti–Ti or Ti–Si bonds contributing to the peak at 454 eV in Fig. 6(a). A peak at ~98 eV corresponding to Si–Si or Si–Ti can also be observed in the Si2p spectra. The presence of Ti, and of potentially intermetallic $TiSi_x$ phases, is consistent with XRD results for the $pN_2 = 0$ Pa sample, where also no diffraction peaks from Si are present. The slight shift of some of the XPS peaks toward lower binding energy relative to references is likely the effect of different charging states compared to the phase or region with C–C bonds used for binding energy calibration. In the two samples with intermediate N content, deposited at $pN_2 = 0.25$ and 0.5 Pa, the Ti–C peaks in Ti2p and C1s spectra are shifted about 0.5 eV toward higher binding energy. This can be explained by a decreased net negative charge density on Ti and C atoms in the Ti–C lattice, caused by nitridation. As N has a higher electronegativity than C, the corresponding Ti2p and C1s core levels experience a shift towards higher binding energy as N substitutes C in the Ti–C–N lattice. The trend toward an XPS spectrum of a more TiN-like character at higher $N_2$ deposition pressure is supported by the shift of the Ti(C,N) 220 XRD diffraction peak toward the TiN reference position at high N content (Fig. 3). In the N1s spectra, Ti–N bonds appear with a slight broadening toward lower binding energy at increased N content, which is likely an effect of C. Bonding in the quarternary system can thus be described as a carbonitride, in the sense that the presence of N affects C and vice versa. Since the crystalline structure is TiN-like NaCl-structure, we suggest simultaneous solid solubility of Si on the Ti sublattice and C on the N sublattice into combined (Ti,Si)(C,N), which constitutes the nanosized grains in the structure.

At still higher N content, in the samples deposited at $pN_2 = 2$ and 6 Pa, the Ti–C components vanish from the XPS profile, indicating that Ti has a clear bonding preference for N rather than C. These N levels correspond to compositional saturation as determined by ERDA. Still, the N1s core level signal assigned to Ti–N at ~397 eV is most intense for the 0.25 and 0.5 Pa samples, and with increasing N content the peak is broadened toward lower binding energies. Simultaneously, a broad peak at ~399 eV emerges in the N1s spectra. This feature is attributed to $C–N_x$ type bonds, which are reported around 400 eV binding energy depending on the type of hybridization.[28] Such C–N bonds would also be responsible for the shoulder at 286 eV in the C1s spectra, and of higher intensity with increasing N content. Signs of C–N bonds on the C1s peak have previously been reported in Ti–Si–C–N[8] and Ti–C–N[29] films, where C–C and C–N bonds are allegedly present in an amorphous matrix surrounding 5–15 nm large Ti(C,N) grains.[29] These reports do not, however, identify corresponding peaks in the N1s spectra, despite that this is a determining peak for $CN_x$.[28,30] This suggests that our clear features at ~400 eV correspond to a comparatively higher amount of C–N bonds. Nevertheless, the relative volume and ordering of $CN_x$ compounds must be limited as no electron diffraction[31] intensity was revealed from the samples (Fig. 4).

The peak from C–C bonds at 284.6 eV is dominant in the C1s spectra and to a large extent caused by surface contamination. Hence, no information is given about presence or prevalence of C–C bonds in film. There are also $Ti2p_{3/2}$ peaks present from $TiO_2$ at 459 eV and an oxynitride, $TiO_xN_y$, at ~456.5 eV, causing the plateau-like shape in the $Ti2p_{3/2}$ spectra for the $pN_2 = 2$ and 6 Pa samples.

The Si2p profile for the $pN_2 = 0$ Pa sample has, in addition to the broad peak at ~98 eV, a second peak at ~102 eV corresponding to Si–N bonds, as in $Si_3N_4$. With increasing $N_2$ deposition pressure, the Si–N peak is broadened and shifted toward lower binding energies, indicating the formation of Si–C bonds. Furthermore, in the N1s spectra, Si–N bonds might also be present as a minor component at 398 eV, between the Ti–N and $C–N_x$ peaks. The formation of $Si_3N_4$, previously reported in the quarternary system studied here,[3,7,9] is thus possible but not dominating. In our experiments, no signature of $Si_3N_4$ was detected from XRD, indicating that the phase, if present, is amorphous.

### D. Surface morphology

The surface morphology of the films, as imaged by SEM in Fig. 7, changes from rather smooth for intermediate N content, to very rough at the high end of the $N_2$ deposition pressure. At $pN_2 = 6$ Pa, the surface has a rugged structure, which can be correlated with the undulating growth layers in Fig. 5, where the segregation of light elements is destined for the valleys. The rough surface morphology is connected with the limited surface diffusion as a result of low growth temperature and low energy flux[32] applied here, and the effect of macroparticle incorporation resulting from arc deposition.[33] Hence, the change in morphology can also be explained by the generally observed decrease in ion flux and ion energy with increasing deposition pressure (see, for example, Ref. 34), limiting the total energy supplied to the surface. The segregation and the dense crystalline structure determined by TEM do, however, suggest some surface diffusion.

### E. Mechanical properties

The hardness of the films is presented in Fig. 2(b). The film deposited at $pN_2 = 0$ Pa, with partly carbide character, shows a modest hardness of 27 GPa, somewhat higher than Ti–Si–C nanocomposite films (20 GPa),[35] but lower compared to TiC films (36 GPa).[2] Hence, the film structure may be weakened by the presence of Ti and $TiSi_x$ phases. The enhanced hardness, up to 49 GPa, at intermediate N content, can be explained by the feathered microstructure of highly ordered small grains with strong interconnection that restrict movement of grains and

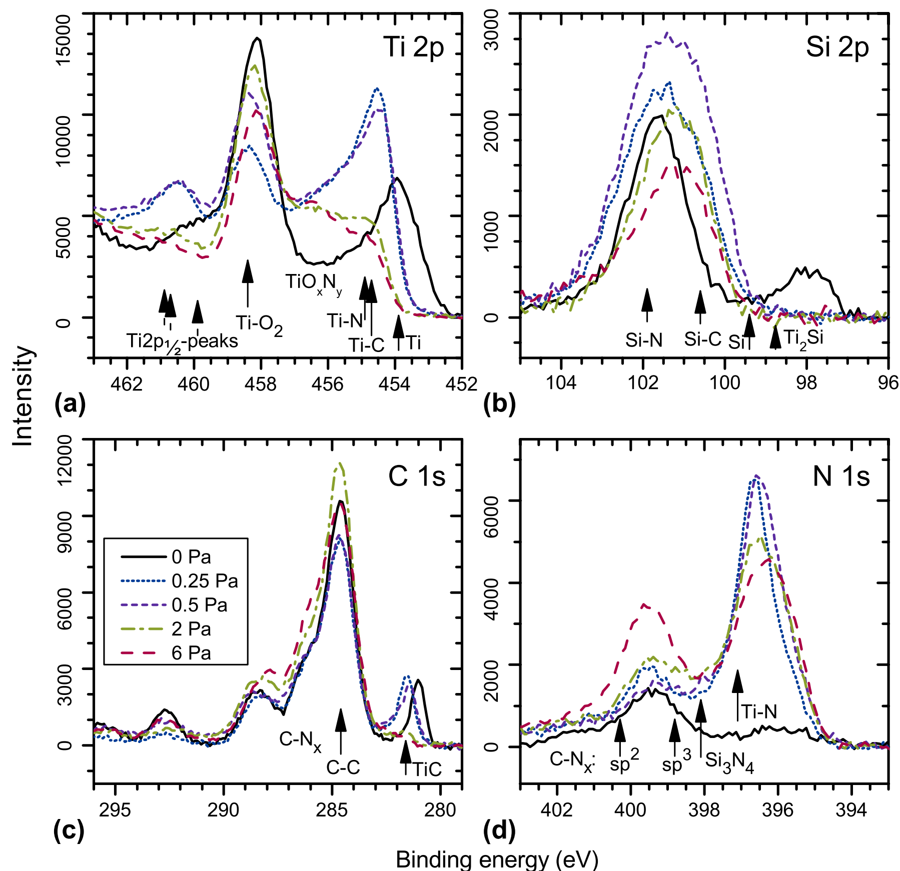


FIG. 6. X-ray photoelectron spectroscopy peak profiles from samples grown at different $N_2$ pressures.

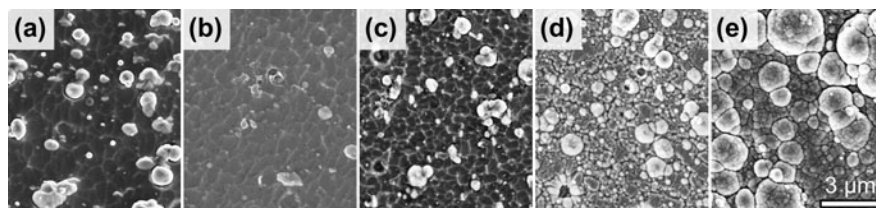


FIG. 7. Scanning electron microscope images from Ti–Si–C–N films grown at $pN_2$ equal to (a) 0 Pa, (b) 0.25 Pa, (c) 0.5 Pa, (d) 2 Pa, and (e) 6 Pa.

dislocations in response to deformation. These properties may be further enhanced by Si- and C-rich tissue phases, as seen in Ti–Si–N.[1] For the $pN_2 = 6$ Pa sample, the decreased hardness is combined with loss of the strong directional bonding present in the feathered structure at lower N content. The grain orientation is random, typically with high-angle grain boundaries [Fig. 4(c)]. We suggest that the cohesion of the material is weakened by the segregating grain boundary phases.

The hardness maximum covers the region where the feathered structure was detected in TEM and where the XPS results indicate a Ti–Si–C–N solid solution. Arc-deposited Ti–Si–N films have been reported with a maximum hardness of 42 GPa, corresponding to a Si-content of 6.5 at%, where the hardening was attributed to defects, solid solution, grain size, and coherency strain with crystalline $SiN_x$ at grain boundaries.[1] Similar hardness, 38–40 GPa, was also found in arc-deposited Ti–Si–C–N films from binary Ti–Si cathodes.[16] In both cases, the films exhibit the feather-like microstructure. For PECVD-grown Ti–Si–C–N-films, hardness up to 48 GPa has been reported under C-rich conditions for which a structure forms with nanocrystalline Ti(C,N) and amorphous C and $Si_3N_4$.[7]

Previous reports on Ti–C–N films discuss different hardening mechanisms. Lu et al.[29] investigated Ti–C–N coatings with various C content grown by reactive unbalanced magnetron sputtering. The maximum hardness of 49 GPa was obtained for 12.5 at.% C, attributed to solid-solution hardening and high residual stress. At higher C content, a nanocomposite structure was formed, consisting of Ti(C,N) grains in an amorphous matrix containing C and $CN_x$, with drastically lower hardness and compressive stress.[29] Arc-deposited Ti–C–N films with a maximum hardness of 45 GPa, corresponding to a C content of ~28 at.%, were studied by Karlsson et al.[2] The hardness was explained by an increasing bond strength as the covalent character increases when C replaces N, combined with strain induced by defect density, which was found largest in the range of maximum hardness. In our case, all samples exhibit significant defect density, relatively high residual stress, and small grain size, all of which likely contributes to the detected film hardness. The difference between our samples is, however, primarily related to the microstructural differences induced by a changed composition.

### F. Segregation of Si and C in the Ti–Si–C–N films

Films deposited with the $Ti_3SiC_2$ compound cathodes are rich in Si and C, each of which are known to enhance mechanical properties of TiN by promoting grain refinement and defect generation. Our results show that with simultaneous high content of Si and C, the amount of N requires delicate control to avoid segregation and precipitation of weak grain boundary phases based on Si, C, and N. As evident from XRD and TEM analysis, the film growth promotes the B1 NaCl-structure, which cannot accommodate all compositions tested in this study. In growth without $N_2$, the film can be considered to consist of understoichiometric $TiC_x$, with possible Si substitutions together with Ti and silicide phases.

In the partially nitrided films, deposited at $pN_2 = 0.25$ and 0.5 Pa, the cubic-phase (Ti,Si)(C,N) grains arrange in the feathered structure known from Ti–Si–N. Grains are needle-like here, as a result of surface-diffusion mediated segregation that limits lateral grain growth, and with grown-in defects that form semicoherent sub-grains. As discussed in Ref. 1, epitaxial monolayer-thick tissue phases of $SiN_x$ may be formed.

At higher N content, $pN_2 = 6$ Pa, the segregation of Si and C is so extensive that it leads to the formation of nanometer-thick grain boundary phases of $CN_x$ and possibly $Si_3N_4$ as determined by STEM and XPS analysis. At the same time, the renucleation rate of the cubic phase on the film surface increases, resulting in an equiaxed grain structure with no preferential orientation in these samples. Since $CN_x$ (and $Si_3N_4$) are incoherent phases with lower hardness than the cubic Ti(C,N), this extensive segregation reduces the total film hardness. Thus, in abundance of N, the combined presence of Si and C disturbs cubic phase growth severely and compromises mechanical strength of the films.

## IV. CONCLUSIONS

Predominantly cubic Ti–Si–C–N alloy thin films with a wide range of compositions can be deposited by arc evaporation from $Ti_3SiC_2$ compound cathodes at varying $N_2$ pressures. Without reactive gas, the films consist of a mixture of $TiC_x$ and metallic phases (Ti, $TiSi_x$) and have a moderate hardness of 27 GPa. Superhard, up to 49 GPa, (Ti,Si)(C,N) films with a nanocrystalline feathered structure of primarily cubic phase form at $pN_2 = 0.25$–0.5 Pa. Above $pN_2 = 2$ Pa, which corresponds to saturation of N content, the crystalline phases obtain a pronounced nitride character. At the same time, C and Si segregate to microscopic column and nanoscopic grain boundaries, which weaken the material's strength.

While Si and C added separately have beneficial effects on the hardening of TiN through effective grain refinement and solid solution hardening, their combined presence in high concentrations, together with N, accelerates the phase separation into incoherent $CN_x$ and possibly $Si_3N_4$ and thus degrades the mechanical properties of Ti–Si–C–N films.

## ACKNOWLEDGMENTS

This work was funded by the VINN Excellence center on Functional Nanoscale Materials (FunMat). The

authors also acknowledge Uppsala University for access to the Tandem Laboratory for ERDA analysis.

## REFERENCES


1. A. Flink, M. Beckers, J. Sjölen, T. Larsson, S. Braun, L. Karlsson, and L. Hultman: The location and effects of Si in $(Ti_{1-x}Si_x)N_y$ thin films. *J. Mater. Res.* **24**, 2483 (2009).
2. L. Karlsson, L. Hultman, M.P. Johansson, J.E. Sundgren, and H. Ljungcrantz: Growth, microstructure, and mechanical properties of arc evaporated $TiC_xN_{1-x}$ ($0 \leq x \leq 1$) films. *Surf. Coat. Techol.* **126**, 1 (2000).
3. S. Abraham, E.Y. Choi, N. Kang, and K.H. Kim: Microstructure and mechanical properties of Ti-Si-C-N films synthesized by plasma-enhanced chemical vapor deposition. *Surf. Coat. Techol.* **202**, 915 (2007).
4. D.-H. Kuo and K.-W. Huang: A new class of Ti-Si-C-N coatings obtained by chemical vapor deposition, Part 1: 1000 °C process. *Thin Solid Films* **394**, 72 (2001).
5. D.-H. Kuo and K.-W. Huang: A new class of Ti-Si-C-N coatings obtained by chemical vapor deposition—Part II: Low-temperature process. *Thin Solid Films* **394**, 81 (2001).
6. D.-H. Kuo and W.-C. Liao: A new class of Ti-Si-C-N coatings obtained by chemical vapor deposition, Part III: 650–800 °C process. *Thin Solid Films* **419**, 11 (2002).
7. Y. Guo, S.L. Ma, and K.W. Xu: Effects of carbon content and annealing temperature on the microstructure and hardness of super hard Ti-Si-C-N nanocomposite coatings prepared by pulsed d.c. PCVD. *Surf. Coat. Techol.* **201**, 5240 (2007).
8. P. Jedrzejowski, J.E. Klemberg-Sapieha, and L. Martinu: Quaternary hard nanocomposite $TiC_xN_y$/SiCN coatings prepared by plasma enhanced chemical vapor deposition. *Thin Solid Films* **466**, 189 (2004).
9. D.Y. Ma, S.L. Ma, H.S. Dong, K.W. Xu, and T. Bell: Microstructure and tribological behavior of super-hard Ti-Si-C-N nanocomposite coatings deposited by plasma enhanced chemical vapour deposition. *Thin Solid Films* **496**, 438 (2006).
10. D.Y. Ma, S.L. Ma, and K.W. Xu: Superhard nanocomposite Ti-Si-C-N coatings prepared by pulsed-d.c plasma enhanced CVD. *Surf. Coat. Techol.* **200**, 382 (2005).
11. D.V. Shtansky, E.A. Levashov, A.N. Sheveiko, and J.J. Moore: The structure and properties of Ti-B-N, Ti-Si-B-N, Ti-Si-C-N, and Ti-Al-C-N coatings deposited by magnetron sputtering using composite targets produced by self-propagating high-temperature synthesis (SHS). *J. Mater. Synth. Process.* **6**, 61 (1998).
12. D.V. Shtansky, E.A. Levashov, A.N. Sheveiko, and J.J. Moore: Synthesis and characterization of Ti-Si-C-N films. *Metall. Mater. Trans. A* **30**, 2439 (1999).
13. H. Xu, X. Nie, and R. Wei: Tribological behavior of a TiSiCN coating tested in air and coolant. *Surf. Coat. Techol.* **201**, 4236 (2006).
14. R.H. Wei, E. Langa, C. Rincon, and J.H. Arps: Deposition of thick nitrides and carbonitrides for sand erosion protection. *Surf. Coat. Techol.* **201**, 4453 (2006).
15. J.-H. Jeon, S.R. Choi, W.S. Chung, and K.H. Kim: Synthesis and characterization of quaternary Ti-Si-C-N coatings prepared by a hybrid deposition technique. *Surf. Coat. Techol.* **188–189**, 415 (2004).
16. L.J.S. Johnson, L. Rogström, M.P. Johansson, M. Odén, and L. Hultman: Microstructure evolution and age hardening in (Ti, Si)(C, N) thin films deposited by cathodic arc evaporation. *Thin Solid Films* **519**, 1397 (2010).
17. C.-L. Chang and T.-J. Hsieh: Effect of $C_2H_2$ gas flow rate on synthesis and characteristics of Ti-Si-C-N coating by cathodic arc plasma evaporation. *J. Mater. Process. Technol.* **209**, 5521 (2009).
18. M.W. Barsoum: A new class of solids: Thermodynamically stable nanolaminates. *Prog. Solid State Chem.* **28**, 201 (2000).
19. M.S. Jansson: CONTES, Conversion of Time-Energy Spectra—a Program for ERDA Data Analysis, Uppsala University, 2004.
20. W.C. Oliver and G.M. Pharr: An improved technique for determining hardness and elastic-modulus using load and displacement sensing indentation experiments. *J. Mater. Res.* **7**, 1564 (1992).
21. A.O. Eriksson, J.Q. Zhu, N. Ghafoor, M.P. Johansson, J. Sjölén, J. Jensen, M. Odén, L. Hultman, and J. Rosén: Layer formation by resputtering in Ti-Si-C hard coatings during large scale cathodic arc deposition. *Surf. Coat. Technol.* DOI: 10.1016/j.surfcoat.2011.02.007 (2011).
22. Y. Guo, S.L. Ma, K.W. Xu, T. Bell, X.Y. Li, and H.S. Dong: On the oxidation resistance of superhard Ti-Si-C-N coatings.:*J. Mater. Res.* **23**, 2420 (2008).
23. PDF: TiN 00-038-1420, TiC 00-032-1383, Ti 00-044-1294, $TiSi_2$ 00-035-0785, $Ti_5Si_3$ 00-029-1362, ICDD "Powder Diffraction File" (2008).
24. J.A. Sue: X-ray elastic constants and residual stress of textured titanium nitride coating. *Surf. Coat. Techol.* **54–55**, 154 (1992).
25. A. Flink, T. Larsson, J. Sjölen, L. Karlsson, and L. Hultman: Influence of Si on the microstructure of arc evaporated (Ti, Si)N thin films; evidence for cubic solid solutions and their thermal stability. *Surf. Coat. Techol.* **200**, 1535 (2005).
26. T. Marten, E.I. Isaev, B. Alling, L. Hultman, and I.A. Abrikosov: Single-monolayer $SiN_x$ embedded in TiN: A first-principles study. *Phys. Rev. B* **81**, 212102 (2010).
27. L. Hultman, J. Bareño, A. Flink, H. Söderberg, K. Larsson, V. Petrova, M. Odén, J.E. Greene, and I. Petrov: Interface structure in superhard TiN-SiN nanolaminates and nanocomposites: Film growth experiments and ab initio calculations. *Phys. Rev. B* **75**, 155437 (2007).
28. A. Snis and S.F. Matar: Electronic density of states, 1s core-level shifts, and core ionization energies of graphite, diamond, $C_3N_4$ phases, and graphitic $C_{11}N_4$. *Phys. Rev. B* **60**, 10855 (1999).
29. Y.H. Lu, Y.G. Shen, Z.F. Zhou, and K.Y. Li: Phase configuration, nanostructure evolution, and mechanical properties of unbalanced magnetron-sputtered $Ti$-$C_x$-$N_y$ thin films. *J. Vac. Sci. Technol. A* **25**, 1539 (2007).
30. N. Hellgren, M.P. Johansson, E. Broitman, L. Hultman, and J.-E. Sundgren: Role of nitrogen in the formation of hard and elastic $CN_x$ thin films by reactive magnetron sputtering. *Phys. Rev. B* **59**, 5162 (1999).
31. J. Neidhardt, L. Hultman, and Z. Czigány: Correlated high resolution transmission electron microscopy and x-ray photoelectron spectroscopy studies of structured $CN_x$ ($0 < x < 0.25$) thin solid films. *Carbon* **42**, 2729 (2004).
32. A. Anders: A structure zone diagram including plasma-based deposition and ion etching. *Thin Solid Films* **518**, 4087 (2010).
33. A. Anders: *Cathodic Arcs*, Chapter 6(Springer, New York, 2008).
34. J. Rosén, A. Anders, S. Mraz, A. Atiser, and J.M. Schneider: Influence of argon and oxygen on charge-state-resolved ion-energy distributions of filtered aluminum arcs. *J. Appl. Phys.* **99**, 123303 (2006).
35. P. Eklund: Novel ceramic Ti-Si-C nanocomposite coatings for electrical contact applications. *Surf. Eng.* **23**, 406 (2007).